Journal of Materials Chemistry A

ROYAL SOCIETY OF CHEMISTRY

PAPER

View Article Online
View Journal | View Issue

Cite this: J. Mater. Chem. A, 2025, 13, 14346

Synergistic engineering of micron-sized porous silicon anodes *via* Ge doping and liquid metal alloy modification for high-energy-density lithium-ion batteries†

Lin Sun, *[ab] Lijun Wang,[ab] Yang Liu,[a] Hongyu Wang[a] and Zhong Jin *[b]

In contrast to nanosilicon, micron-sized silicon anodes have gained widespread attention due to their high energy density, favorable processability, and reduced side reactions. However, these anodes are plagued by several significant challenges. They undergo substantial volume changes, and suffer from sluggish lithium-ion transport kinetics and the loss of electrical contact. In this study, micron-sized porous silicon (pSi) obtained through acid etching of an $Al_{60}Si_{40}$ alloy was utilized as the starting material. A novel approach combining high-energy ball milling and wet chemistry methods was adopted to dope Ge atoms into pSi and modify it with a liquid GaInSn metal (LM) alloy (designated as pSi/Ge@LM). The incorporation of Ge heteroatoms and LM offers multiple benefits. Firstly, it enhances the tap density of pSi. Secondly, it effectively boosts the electron transport performance of the material. Moreover, the excellent metallic properties and liquid fluidity of LM endow it with a unique "self-healing" function. Both the half-cells and full-cells assembled with the pSi/Ge@LM electrode demonstrate outstanding electrochemical performance. Specifically, in the half-cells, when cycled at a current density of 1 A g^{-1} for 400 times, the pSi/Ge@LM electrode retains a remarkably high specific capacity of 1011 mA h g^{-1}. Even at a high current density of 3 A g^{-1}, it still delivers a reversible capacity of over 900 mA h g^{-1}. It is anticipated that this research will offer novel insights and valuable guidance for the development of high-energy-density micron-sized silicon anodes.

Received 12th January 2025
Accepted 31st March 2025

DOI: 10.1039/d5ta00298b

rsc.li/materials-a

1 Introduction

Constrained by the relatively low theoretical capacity of graphite (approximately 372 mA h g^{-1}), lithium-ion batteries (LIBs) employing graphite anodes are no longer able to satisfy the burgeoning demands of electric vehicles with extended driving ranges, portable electronic devices, and grid-energy storage. Consequently, the development of novel high-capacity anode materials has become an extremely pressing task.[1] Silicon (Si) anode materials stand out with a remarkably theoretical specific capacity (~4200 mA h g^{-1}, which is tenfold that of graphite), a relatively low working potential, abundant reserves, and environmental friendliness.[2,3] As such, Si is one of the most promising candidates to substitute commercial graphite. However, the widespread application of Si anodes is hampered by their poor electrical conductivity, substantial volume expansion, and unstable solid–liquid interfaces.[4–6]

To alleviate the volume expansion of Si and enhance the stability of the electrode, the commonly adopted strategies are nanosizing combined with coating,[7–9] as well as modifying binders[10–12] and electrolytes.[13–15] Specifically, reducing the size of Si to the nanoscale at a critical value can effectively impede the crack propagation induced by the volume expansion of Si and thus enhance the stability of the electrodes.[16,17] Nevertheless, it should be noted that considering the requirements of commercial LIBs for high gravimetric/volumetric specific energy density, coulombic efficiency, electrode areal density, and electrode thickness, an assessment reveals that the currently reported nano-Si materials fall short of meeting these demands.[18,19]

In light of this, in recent years, as researchers have come to realize that laboratory-level nano-Si anode materials lack the potential for large-scale commercial applications, they have refocused their attention on micron-sized Si-based anode

[a]School of Chemistry and Chemical Engineering, Yancheng Institute of Technology, Yancheng, 224051, China

[b]State Key Laboratory of Coordination Chemistry, MOE Key Laboratory of Mesoscopic Chemistry, MOE Key Laboratory of High Performance Polymer Materials and Technology, Jiangsu Key Laboratory of Advanced Organic Materials, Suzhou Key Laboratory of Green Intelligent Manufacturing of New Energy Materials and Devices, Tianchang New Materials and Energy Technology Research Center, Institute of Green Chemistry and Engineering, School of Chemistry and Chemical Engineering, Nanjing University, Nanjing, Jiangsu 210023, P. R. China. E-mail: sunlin@nju.edu.cn; zhongjin@nju.edu.cn

† Electronic supplementary information (ESI) available: Experimental details, XRD patterns, SEM images, BET data, EDS spectra, cell data and digital photographs. See DOI: https://doi.org/10.1039/d5ta00298b

materials in an effort to improve their comprehensive electrochemical performance.[20,21] For instance, Guo *et al.* adopted an *in situ* magnesium doping strategy to construct a closed nanopore structure within micron-sized SiO_x. The introduced magnesium atoms can facilitate the segregation of oxygen, leading to the formation of a high-density magnesium silicate phase. Simultaneously, due to the consumption of irreversible oxygen by magnesium doping, the initial coulombic efficiency (ICE) of the electrodes has been notably enhanced.[22] Given that micron-sized Si materials have relatively large particle sizes, their volume change rates during the charging and discharging processes are much greater than those of nanosized Si materials. Therefore, it is of utmost importance to mitigate the volume expansion of micron-sized Si materials and improve the electrical conductivity of the electrodes through effective means to enhance their stability.[23]

In this study, we prepared micron-sized porous Si (pSi) materials *via* acid-etching of commercial silicon–aluminum ($Al_{60}Si_{40}$) alloys. Subsequently, metal Ge atoms were doped into pSi through ball-milling. Additionally, we introduced a liquid metal GaInSn alloy (LM) into the pSi to obtain a composite material (designated as pSi/Ge@LM). The introduction of Ge atoms and LM can synergistically enhance the electrical conductivity and increase the tap density of the pSi-based electrode. Moreover, since LM exhibits both metallic and fluid properties, leveraging its unique "self-healing" characteristics, it can effectively rectify the poor electrical contact resulting from particle fragmentation during the repeated charging and discharging processes. Benefiting from the synergistic effect of metal Ge atoms and LM, the half-cells assembled with pSi/Ge@LM as the anode and metal Li as the counter electrode demonstrated significantly improved electrochemical performance. Specifically, it achieved a reversible specific capacity exceeding 2000 mA h g^{-1} at a current density of 0.2 A g^{-1} and a capacity retention rate exceeding 85% after 100 cycles. We believe that this work can offer valuable insights for the development of high-performance micron-sized Si-based anode materials.

2 Results and discussion

The schematic diagram for the synthesis of the pSi/Ge@LM sample is depicted in Fig. 1a. Initially, a micrometer-sized $Al_{60}Si_{40}$ alloy was employed as the raw material, and porous silicon (pSi) was prepared by etching the aluminum (Al) component with hydrochloric acid. The phase structure and morphology of the $Al_{60}Si_{40}$ alloy are presented in Fig. S1.† As evident from Fig. S1a,† all the diffraction peaks of the $Al_{60}Si_{40}$ alloy precisely match the standard peaks of Si (PDF card 27-1402) and Al (PDF card 04-0787), with no detection of other impurity phases. Fig. S1b and c† illustrate that the $Al_{60}Si_{40}$ alloy exhibits a nearly spherical morphology, with a diameter ranging from approximately 1–5 μm. Following the hydrochloric acid etching treatment, the X-ray diffraction (XRD) patterns and scanning electron microscopy (SEM) images of the obtained pSi are shown in Fig. S2.† It is clearly observable that after the acid treatment, the Al in the alloy has been completely removed.

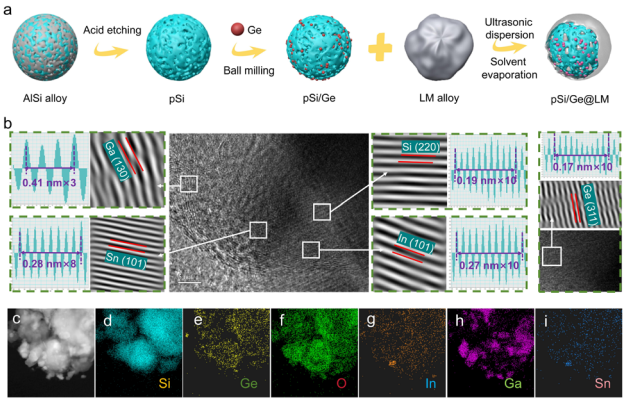

Fig. 1 (a) Schematic illustration of the preparation of pSi/Ge@LM; (b) HRTEM images of the pSi/Ge@LM sample; (c–i) the TEM image and the corresponding elemental mappings of pSi/Ge@LM.

Consequently, the particle morphology has transformed from a smooth spherical shape to a porous one, as depicted in Fig. S2b and c.† Fig. S3† presents the nitrogen isothermal adsorption–desorption curve and the pore size distribution curve of the pSi sample. The Brunauer–Emmett–Teller (BET) specific surface area of pSi reaches 31.7 m^2 g^{-1} (Fig. S3a†), and it exhibits a distinct macropore distribution (Fig. S3b†). This is primarily attributed to the fact that upon the removal of Al from the alloy, Al acts as a self-template, leaving vacancies within the silicon material and thereby forming the characteristic porous structure.

To enhance the cycling stability and improve the ion and electron transport properties of the pSi anode, metal germanium (Ge) atoms were successively doped into pSi, and a liquid gallium (Ga)–indium (In)–tin (Sn) ternary metal alloy (LM, with the mass fractions of Ga, In, and Sn being 68.5%, 21.5%, and 10%, respectively) was introduced into pSi *via* ball milling and ultrasonic solution evaporation techniques. The electron micrograph of the LM utilized in this study is shown in Fig. S4.† It can be noted that the prepared LM possesses the fluidity of a liquid and can form a uniform dispersion after sonication in isopropanol. After doping Ge atoms into pSi through ball milling, the SEM images and the corresponding element distribution of the resulting pSi/Ge are presented in Fig. S5.† The particle size after ball milling has decreased, and the Ge atoms are relatively uniformly dispersed within pSi. Subsequently, LM was introduced into the pSi/Ge sample *via* a wet-chemistry approach. Due to the fluid nature of LM, it can penetrate into the interior of pSi.

The morphology and elemental distribution of the obtained pSi/Ge@LM sample are presented in Fig. S6, S7,† and 1b. From the SEM images at different resolutions in Fig. S6,† numerous smaller particles are observed on the surface of the pSi/Ge particles. Fig. S7† indicates that all atoms of LM, along with Ge atoms, are uniformly distributed within pSi. Moreover, from the high-magnification transmission electron microscopy (TEM) image in Fig. 1b, the lattice fringes of each metal in LM, as well as those of Si and Ge, are clearly discernible. The exposed crystal planes of Si and Ge are (220) and (311),

respectively. Fig. 1c–i display the TEM images and the corresponding elemental distributions of the pSi/Ge@LM sample. Similar to the findings in Fig. S7,† these figures reveal that Ge and each metal element in LM are uniformly distributed within the pSi sample. This further demonstrates that the ball milling and ultrasonic evaporation solution methods can effectively introduce uniformly distributed metal Ge atoms and LM into the pSi material.

The phase structure, surface area, surface elemental composition, and valence state information of the obtained samples were comprehensively analyzed by XRD, Raman, N_2 adsorption–desorption, and X-ray photoelectron spectroscopy (XPS) techniques, as depicted in Fig. 2. Fig. 2a displays the XRD patterns of the pSi/Ge@LM sample, along with the comparative samples of pSi/Ge and pSi@LM. Evidently, the positions of the diffraction peaks in the XRD patterns of the pSi/Ge and pSi/Ge@LM samples are in complete accordance with the standard PDF cards of Si#27-1402 and Ge#04-0545. Notably, upon further introduction of LM into the samples, only a diffraction peak with a relatively broad full width at half maximum emerges in the range of 30–35°, corresponding to LM, as presented in the partially enlarged inset of Fig. 2a. This phenomenon is primarily attributed to the amorphous nature of LM in its liquid state.[24,25] Additionally, the elemental distribution of the comparative sample pSi@LM (Fig. S8†) further validates the successful incorporation of LM.

Fig. 2b shows the Raman spectra of the pSi/Ge@LM and pSi@LM samples. The Raman peaks detected at 507 and 930 cm^{-1} for both samples correspond to Si–Si and Si–O, respectively. Moreover, for the pSi/Ge@LM sample, a relatively stronger Raman peak is detected at 300 cm^{-1}, which is associated with the introduction of metallic Ge.[26]

The N_2 isothermal adsorption–desorption curve and pore size distribution curve of the pSi/Ge@LM sample are shown in Fig. 2c and S9,† respectively. It can be observed that after modification with Ge and LM, the Brunauer–Emmett–Teller (BET) specific surface area of pSi/Ge@LM is 8.4 $m^2 g^{-1}$, significantly lower than that of pSi (31.7 $m^2 g^{-1}$). The pore size distribution curve in Fig. S9† clearly indicates that the pSi/Ge@LM sample exhibits no distinct pore characteristics. This suggests that the introduced LM permeates into the interior of pSi and blocks the original macropores of pSi. Consequently, this substantially increases the tap density of the material, which is beneficial to the overall energy density of the battery.

To analyze the elemental composition and valence state information on the surface of the pSi/Ge@LM sample, Fig. 2d–i present the XPS spectra of pSi/Ge@LM. In the XPS full spectrum presented in Fig. 2d, elements such as Si, Ge, Ga, In, and Sn are detected, with scarcely any other impurity peaks. Fig. 2e depicts the high-resolution XPS spectrum of Si 2p, which can be deconvoluted into three peaks located at 98.5, 102.9, and 106.1 eV. These peaks are attributed to Si^0, SiO_x ($0 < x < 2$), and SiO_2,[27,28] respectively. Fig. 2f shows the XPS spectrum of Ge 2p. The deconvoluted peaks located at 1219.3 and 1250.5 eV correspond to Ge^0, while the peaks located at 1220.6 and 1251.6 eV correspond to Ge^{4+}.[29] Furthermore, in the high-resolution XPS spectra of the In, Ga, and Sn elements, as presented in Fig. 2g–i, the corresponding zero-valent metals and partially oxidized states are also observed.

To validate the potential application of pSi/Ge@LM samples as anodes for advanced LIBs, a comprehensive series of electrochemical tests were carried out. Fig. 3a illustrates the cyclic voltammetry (CV) curves of the pSi/Ge@LM electrode within

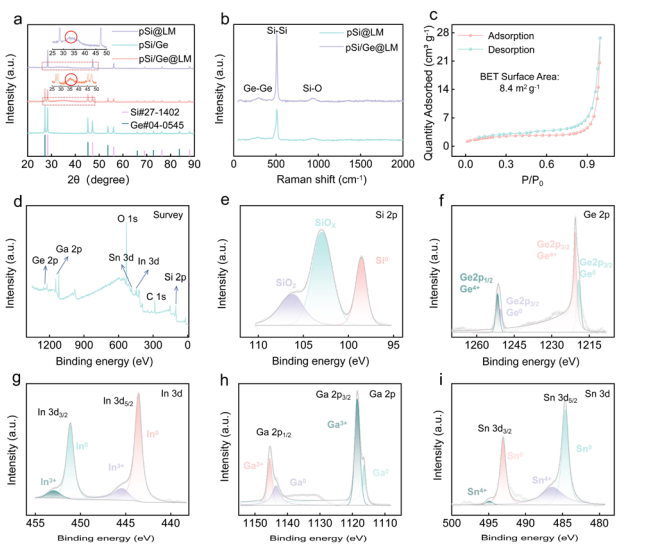

Fig. 2 (a) XRD patterns of the samples of pSi@LM, pSi/Ge and pSi/Ge@LM; (b) Raman spectra of pSi@LM and pSi/Ge@LM; (c) nitrogen isothermal adsorption–desorption curves of pSi/Ge@LM at 77 K; (d–i) XPS spectra of pSi/Ge@LM: (d) survey, (e) Si 2p, (f) Ge 2p, (g) In 3d, (h) Ga 2p, and (i) Sn 3d.

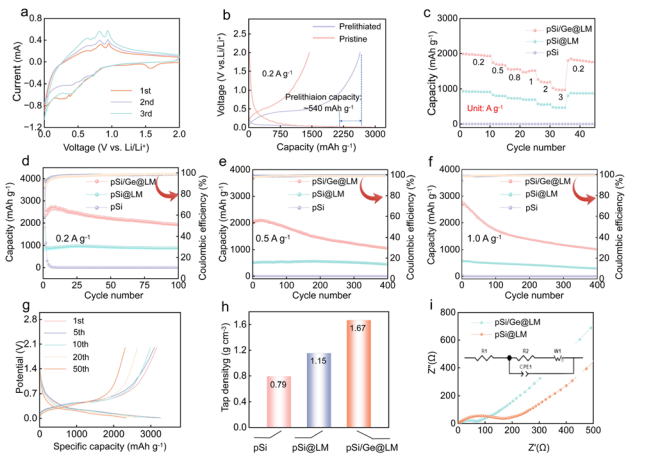

Fig. 3 (a) CV curves of the pSi/Ge@LM electrode in the first three cycles; (b) charge–discharge curves of the pSi/Ge@LM electrode in the first cycle before and after prelithiation; (c) rate performance of the pSi, pSi@LM and pSi/Ge@LM electrodes; (d–f) cycling stability tests of the pSi, pSi@LM and pSi/Ge@LM electrodes at different current densities; (g) charge–discharge curves of the pSi/Ge@LM electrode at different cycle numbers; (h) comparison of the tap density of the pSi, pSi@LM and pSi/Ge@LM materials; (i) electrochemical impedance spectra (EIS) of the pSi@LM and pSi/Ge@LM electrodes and the corresponding equivalent circuit diagrams.

a potential window of 0–2.0 V for the initial three cycles. Evidently, the irreversible cathodic peak appearing at approximately 1.55 V during the first discharge process can be ascribed to the formation of the SEI film.[30,31] The reversible peak at 0.73 V corresponds to the alloying reaction between metal Ga with Li, and the reversible peak at 0.41 V is associated with the lithium-intercalation process of metal Sn.[32] During the charging process, four relatively distinct anodic peaks appear at 0.62 V, 0.72 V, 0.84 V and 0.94 V. These peaks can be respectively attributed to the delithiation process of Si/Ge and the delithiation process of LM.[33] For comparison, the CV curves of the pSi@LM electrode for the first three cycles are presented in Fig. S10.† It is clear that the cathodic and anodic peaks that emerge are similar to those of the pSi/Ge@LM electrode, indicating that the pSi/Ge@LM and pSi@LM electrodes share the same working mechanism. In order to further analyze the embedded delithiation mechanism of the material, we characterized and analyzed the XRD patterns of the pSi/Ge@LM electrode in different charging and discharging states. Fig. S11† shows the XRD plots of the pSi/Ge@LM electrode in the initial state, discharged state and charged state, respectively. It can be seen that the characteristic peaks of Si, Ge and LM around 35° disappeared during the lithiation process, and a new lithiation peak appeared around 38° instead. The disappearance of Si and Ge diffraction peaks is attributed to the amorphous nature of the formed compounds such as Li–Si. The formation of the new peak at around 38° may be due to the alloying of LM and Li to form new phases such as Li_3In or Li–Ga–In ternary alloys. The reason why this newly generated peak remains in the charging state is that the structure formed by LM and Li may be more stable, which is also consistent with the results of the analysis of CV curves (Fig. 3a).

Fig. 3b shows the voltage profiles of the pSi@LM electrode during the first discharge/charge process before and after prelithiation. The specific discharge and charge capacities of the pristine pSi@LM electrode in the first cycle are 2918 and 1438 mA h g^{-1}, respectively, and the corresponding initial coulombic efficiency (ICE) is merely 49%. After the prelithiation treatment, the discharge and charge capacities in the first cycle are 2643 and 2103 mA h g^{-1}, respectively, and the corresponding ICE value is increased to 80%. This demonstrates that the lithium consumed by the irreversible reaction during the first discharge process can be effectively compensated by a simple prelithiation process. Fig. 3c shows the rate performance of the pSi/Ge@LM electrode and the comparative electrodes. For the pure pSi electrode, the capacity is nearly zero, which is also evident from the subsequent cycling stability tests. This is likely due to the poor electrical conductivity of pSi and numerous side reactions. These factors impede the smooth migration of electrons and ions, resulting in an extremely low capacity. Through the modification of LM, it can be observed that the reversible capacity and rate performance of the pSi/Ge electrode have been significantly enhanced. Further doping with Ge enables the pSi/Ge@LM electrode to exhibit the most outstanding rate performance. Even at a high current density of 3 A g^{-1}, the reversible capacity can still exceed 900 mA h g^{-1}.

Fig. 3d–f display the cycling stability of the pSi/Ge@LM, pSi@LM and pSi electrodes at different current densities. It is observed that the pSi/Ge@LM electrode exhibits the highest reversible specific capacity. Even after 400 cycles of charge and discharge at a current density of 1 A g^{-1}, the specific capacity remains as high as 1011 mA h g^{-1}, while the specific capacity of the pSi@LM electrode is only 292 mA h g^{-1}. The performance of this electrode is comparable to or even better than the related materials reported previously (Table S1†). The results of the cycling stability tests directly confirm the necessity of introducing Ge atoms, which can not only improve the electrical conductivity of the pSi anode but also further enhance its stability during the cycling and increase its reversible capacity.

Moreover, the concurrent introduction of Ge and LM into pSi can effectively augment the tap density of the material, which is conducive to enhancing the energy density of the battery. As shown in Fig. 3h, upon the introduction of LM and Ge into pSi, the tap density of the material increases from 0.79 g cm^{-3} for pSi to 1.15 g cm^{-3} for pSi@LM and 1.67 g cm^{-3} for pSi/Ge@LM, respectively. Additionally, the cycling stability of the pSi/Ge@LM electrode is well maintained (Fig. 3g). To further elucidate the influence mechanism of Ge doping, we measured the Nyquist plots of the pSi/Ge@LM and pSi@LM electrodes before and after cycling, as presented in Fig. 3i and S12.† The insets in the two figures show the corresponding equivalent circuit diagrams, respectively. The Nyquist plots are predominantly composed of two parts: the flattened semicircle in the high-frequency region, representing the charge transfer resistance (R_{ct}), and the sloping line in the low-frequency region, representing the Warburg impedance.[34,35] Based on the test results, regardless of whether it is before or after cycling, the pSi/Ge@LM electrode exhibits a substantially smaller R_{ct} compared to the pSi@LM electrode. This fully demonstrates that even though the doping amount of metal Ge is not substantial, the introduction of Ge plays a pivotal role in enhancing the electron conduction of the entire electrode.

Fig. 4a and b show the schematic diagrams of the different states of pSi and pSi/Ge@LM electrodes after charge–discharge cycles, respectively. These diagrams are designed to more

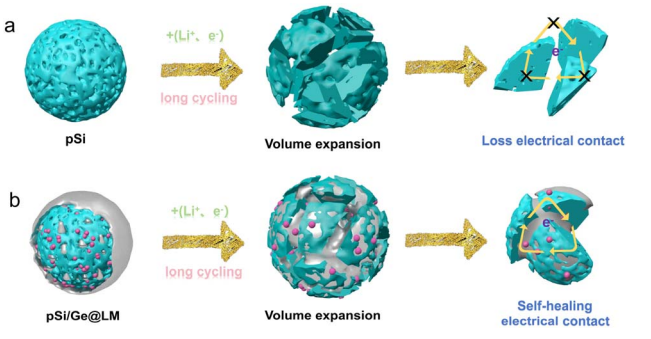

Fig. 4 (a) Schematic diagram of electrode pulverization and loss of electrical contact caused by volume expansion of the pSi electrode after repeated charging and discharging; (b) schematic diagram of the mechanism by which the pSi/Ge@LM electrode benefits from the "self-healing" function of the liquid metal (LM).

vividly demonstrate the performance-improvement mechanism of the pSi electrode simultaneously doped with Ge and modified with LM. Evidently, after undergoing multiple charge–discharge cycles, the pSi electrode will experience cracking, pulverization, and loss of electrical contact due to significant volume expansion, as shown in Fig. 4a. In sharp contrast, as presented in Fig. 4b, although the pSi/Ge@LM electrode also undergoes significant volume changes during the charge–discharge process, owing to the presence of Ge atoms and LM, the electrode can re-establish electrical contact through a self-healing mechanism (indicated by yellow arrows) after volume expansion and structural fragmentation. This self-healing ability enables the electrode to retain effective electrical contact after long-term cycling, thereby optimizing the electrode's performance and preventing the occurrence of electrical deactivation.

To further verify the accuracy of this explanation, we conducted an analysis on the surface and cross-sectional morphologies of the pSi/Ge@LM and pSi@LM electrodes both before and after cycling, as shown in Fig. S13 and S14.† It can be discerned that, in comparison to the pSi@LM electrode, the pSi/Ge@LM electrode exhibits more intact surface integrity and a lower volume expansion rate following cycling. Moreover, for the cycled pSi/Ge@LM electrode, the results of elemental mapping indicate that Ge atoms are relatively evenly distributed on the surface and within Si (Fig. S15†), further attesting to the stability of the electrode.

To delve deeper into the electrochemical kinetics of the electrodes, we measured the CV curves of the pSi/Ge@LM and pSi@LM electrodes at scan rates ranging from 0.2 to 0.6 mV s^{-1}, as shown in Fig. 5a and S17a.† Specifically, the relationship between the peak current (i) and the scan rate (v) can be exploited to investigate the capacitive behavior of the electrode materials. This relationship is described using the following equations:

$$i = av^b \quad (1)$$

$$\log(i) = b\log(v) + \log a \quad (2)$$

where eqn (2) is the logarithmic form of eqn (1). Here, a and b are empirical constants, and the value of b is the slope of the plot of log(i) *versus* log(v), as shown in Fig. 5b. According to the pseudocapacitance theory, when the value of $b = 1$, it implies that the charge storage of the electrode is entirely furnished by the surface pseudocapacitance; when $b = 0.5$, it indicates that the charge storage is predominantly governed by ion diffusion.[36] As shown in Fig. 5b, the b values of Peak 1 and Peak 2 are 0.49 and 0.54, respectively, suggesting that the charge storage of the pSi/Ge@LM electrode is mainly controlled by the diffusion process. This outcome is, in fact, predictable since the pSi/Ge@LM sample does not contain carbon materials, and carbon materials are typically regarded as the primary source for providing pseudocapacitance.[37] Fig. 5c and S17b† show the contributions of pseudocapacitance and ion diffusion to charge storage in the pSi/Ge@LM and pSi@LM electrodes at different scan rates, respectively. It can be seen that the contribution of ion diffusion to charge storage is dominant. Fig. 5d presents the integration result of the CV curve of the pSi/Ge@LM electrode at a scan rate of 0.6 mV s^{-1}. The red and blue regions represent the diffusion-controlled and capacitance-controlled areas of the total stored charge, respectively. The results for other scan rates are shown in Fig. S16.† Compared with the pSi@LM electrode (Fig. S17†), the pSi/Ge@LM electrode has a greater pseudocapacitance contribution at the same scan rate, indicating that the pSi/Ge@LM electrode has better rate performance.

In addition, by employing the galvanostatic intermittent titration technique (GITT) at a current density of 0.05 mA g^{-1}, we investigated the relaxation behavior of the pSi/Ge@LM negative electrode during the charge/discharge process and calculated the lithium-ion diffusion coefficient (Fig. 5e). The calculated lithium-ion diffusion coefficient in the pSi/Ge@LM electrode ranges from 10^{-11} to 10^{-13} cm^2 s^{-1}, which is comparable to that of common Si@C anodes.[38–40] This indicates that the pSi/Ge@LM negative electrode has excellent lithium-ion diffusion ability.

Furthermore, to assess the practical application potential of the pSi/Ge@LM electrode, we conducted a simple performance test of a coin-type full battery with the pSi/Ge@LM electrode serving as the negative electrode and commercial NCM811 as the positive electrode. The schematic diagram of the full battery configuration is shown in Fig. 5f. Fig. 5g depicts the cycle stability test of the full battery at a current density of 0.2 A g^{-1}. After 300 charge–discharge cycles, the full battery still retains a reversible capacity of over 80 mA h g^{-1}. The charge–discharge curves of the battery at different cycle numbers also prove its

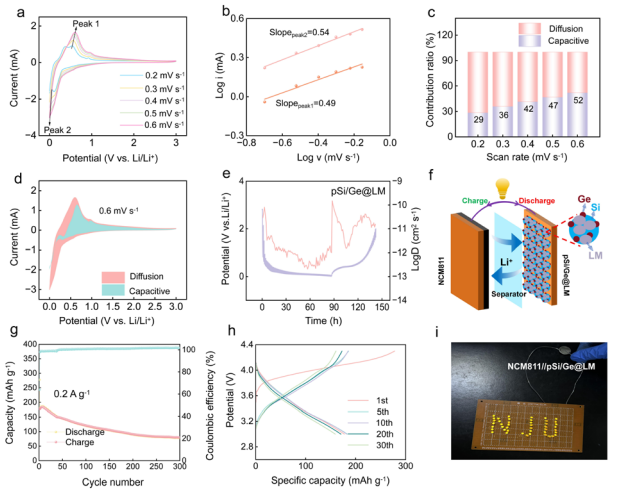

Fig. 5 (a) CV curves of the pSi/Ge@LM electrode at various scan rates; (b) log(v) *vs.* log(i) of each redox peak of the pSi/Ge@LM electrode; (c) the contribution ratios of diffusion and pseudocapacitance to the capacity of the pSi/Ge@LM electrode at different sweep rates; (d) the specific proportion areas of pseudocapacitance and diffusion-controlled processes in the CV graph at a sweep rate of 0.6 mV s^{-1}; (e) Li ion diffusion coefficient curves of the pSi/Ge@LM electrode; (f) schematic diagram of the configuration of a full cell assembled with pSi/Ge@LM as the anode and commercial NCM811 as the cathode. (g) Cycling performance of the full cell at a current density of 0.2 A g^{-1}. (h) Charge–discharge curves of the full cell at different cycle numbers. (i) The pattern composed of 43 LED bulbs illuminated by using the NCM811//pSi/Ge@LM full cell.

good cycle stability (Fig. 5h). Fig. 5i demonstrates that this full battery can effortlessly illuminate a pattern composed of 44 LED bulbs, highlighting its favorable practicality.

3 Conclusions

In this study, we targeted the formidable challenges associated with micron-sized porous silicon (pSi) anodes, namely poor electrical conductivity, low tap density, and severe volume expansion. To surmount these obstacles and improve the electrochemical performance of pSi anodes, we devised a novel strategy involving doping with metal Ge atoms and modification with a liquid metal (LM) alloy. High-energy ball milling technology was employed to dope metal Ge atoms into pSi. Subsequently, taking advantage of the excellent permeability of LM, we synthesized an LM-modified pSi-based anode material, denoted as pSi/Ge@LM, which featured a relatively high tap density. A comprehensive suite of material characterization studies and electrochemical tests were carried out. The results unequivocally demonstrated that the incorporation of Ge atoms significantly enhanced the electrical conductivity of pSi and augmented its reversible capacity. Additionally, owing to the superior metallic conductivity and liquid fluidity of LM, its introduction conferred a "self-healing" property. This property effectively mitigated the volume expansion of pSi and prevented electrical contact deactivation during the charge–discharge process, thereby substantially enhancing the stability of the pSi anode. Benefiting from the synergistic effect of heteroatoms (Ge) and LM, the pSi/Ge@LM electrode exhibited outstanding electrochemical performance. Even after 400 cycles at a high current density of 1 A g^{-1}, the specific capacity of the pSi/Ge@LM electrode remained as high as 1011 mA h g^{-1}. Moreover, in full-cell configurations, pSi/Ge@LM displayed remarkably improved rate performance and excellent electrochemical stability. This research paves the way for the development of next-generation, high-energy-density Si-based anode materials by offering innovative concepts and approaches.

Data availability

The data that support the findings of this study are available from the corresponding author upon reasonable request.

Author contributions

Lin Sun: drafted the manuscript. Lijun Wang, Yang Liu, and Hongyu Wang: designed the experiments and collected data. Zhong Jin and Lin Sun: conceived and obtained funding for this work. Lin Sun: revised the manuscript.

Conflicts of interest

The authors declare that they have no conflict of interest.

Acknowledgements

The authors gratefully acknowledge financial support from the National Natural Science Foundation of China (52202309, 22475096, and 22479074), the Qing Lan Project of Jiangsu Province, the Open Program of State Key Laboratory of Coordination Chemistry (SKLCC2308), the General Project of the Joint Fund of Equipment Pre-research and the Ministry of Education (8091B02052407), the Natural Science Foundation of Jiangsu Province (BK20240400 and BK20241236), the Science and Technology Major Project of Jiangsu Province (BG2024013), the Scientific and Technological Achievements Transformation Special Fund of Jiangsu Province (BA2023037), the Academic Degree and Postgraduate Education Reform Project of Jiangsu Province (JGKT24_C001), the Key Core Technology Open Competition Project of Suzhou City (SYG2024122), the open research fund of Suzhou Laboratory (SZLAB-1308-2024-TS005), the Gusu Leading Talent Program of Scientific and Technological Innovation and Entrepreneurship of Wujiang District in Suzhou City (ZXL2021273), and the Chenzhou National Sustainable Development Agenda Innovation Demonstration Zone Provincial Special Project (2023sfq11).

Notes and references

1 M. Li, R. P. Hicks, Z. Chen, C. Luo, J. Guo, C. Wang and Y. Xu, *Chem. Rev.*, 2023, **123**, 1712–1773.
2 L. Sun, Y. Liu, R. Shao, J. Wu, R. Jiang and Z. Jin, *Energy Storage Mater.*, 2022, **46**, 482–502.
3 L. Sun, Y. Liu, L. Wang and Z. Jin, *Adv. Funct. Mater.*, 2024, **34**, 2403032.
4 H. Kawaura, R. Suzuki, Y. Kondo and Y. Mahara, *ACS Appl. Mater. Interfaces*, 2023, **15**, 34909–34921.
5 M. Li, N. N. Patil, S. Singh, D. McNulty and K. M. Ryan, *J. Mater. Chem. A*, 2025, **13**, 696–703.
6 A. Pendashteh, R. Tomey and J. J. Vilatela, *Adv. Energy Mater.*, 2024, **14**, 2304018.
7 L. Sun, Y. Liu, L. Wang, Z. Chen and Z. Jin, *Nano Res.*, 2024, **17**, 9737–9745.
8 L. Sun, X. Wang, Y. Liu, H. Xu, H. Wang, Y. Lu and Z. Jin, *ACS Appl. Mater. Interfaces*, 2024, **16**, 52349–52357.
9 S. Wu, H. Wu, X. Kong, Y. Li, G. Xu, J. Su, J. Huang, G. Wang and X. Ou, *Chem. Eng. J.*, 2024, **502**, 158032.
10 B. Dong, H. Zhu, X. Cai, C. Guo, Y. Hao and L. Xi, *J. Power Sources*, 2025, **626**, 235745.
11 Z. Liu, Y. Wang, G. Liu, X. Yue, Z. Shi, Y. Tan, J. Zhao, Y. Lei, X. Yan and Z. Liang, *J. Am. Chem. Soc.*, 2024, **146**, 34491–34500.
12 B. Sun, X. Jiao, J. Liu, R. Qiao, C. Mao, T. Zhao, S. Zhou, K. Shi, M. Ravivarma, J. Shi, H. Fan and J. Song, *Nano Lett.*, 2024, **24**, 7662–7671.
13 Z. Cao, X. Zheng, Q. Qu, Y. Huang and H. Zheng, *Adv. Mater.*, 2021, **33**, 2103178.
14 Y. Ko, J. Bae, G. Chen, M. A. Baird, J. Yan, L. Klivansky, D.-M. Kim, S. E. Trask, M.-T. F. Rodrigues, G. M. Carroll, N. R. Neale and B. A. Helms, *ACS Energy Lett.*, 2024, **9**, 3448–3455.

15 J. Pan, H. Lu, D. Wu, N. Wang, Q.-H. Yang and S. Dou, *Energy Storage Mater.*, 2024, **72**, 103701.
16 M. Cai, Z. Zhao, X. Qu, J. Qu, Z. Hu, H. Shi, S. Gao, D. Wang and H. Yin, *Energy Storage Mater.*, 2023, **57**, 568–576.
17 X. Jiang, L. Sun, Y. Lu, H. Wang, J. Shi, L. Yang, L. Zhang, R. Lv and Z. Jin, *J. Power Sources*, 2024, **602**, 234331.
18 Z. Cheng, W. Chen, Y. Zhang, J. Xiang, D. Tang, H. Ji, J. Li, Y. Huang and L. Yuan, *Adv. Funct. Mater.*, 2024, **34**, 2408145.
19 T. Liu, T. Dong, M. Wang, X. Du, Y. Sun, G. Xu, H. Zhang, S. Dong and G. Cui, *Nat Sustainability*, 2024, **7**, 1057–1066.
20 D. Gueon, H. Ren, Z. Sun, B. Mosevitzky Lis, D. D. Nguyen, E. S. Takeuchi, A. C. Marschilok, K. J. Takeuchi and E. Reichmanis, *ACS Appl. Energy Mater.*, 2024, **7**, 7220–7231.
21 Z. Ju, B. Zhang, T. Zheng, A. C. Marschilok, E. S. Takeuchi, K. J. Takeuchi and G. Yu, *Nano Lett.*, 2024, **24**, 6610–6616.
22 D.-X. Xu, Y.-M. Zhao, H.-X. Chen, Z.-Y. Lu, Y.-F. Tian, S. Xin, G. Li and Y.-G. Guo, *Angew. Chem., Int. Ed.*, 2024, **63**, e202401973.
23 Z. Liu, R. Hu, R. Yu, M. Zheng, Y. Zhang, X. Chen, L. Shen and Y. Xia, *Nano Lett.*, 2024, **24**, 4908–4916.
24 C. Wei, H. Fei, Y. Tian, Y. An, H. Guo, J. Feng and Y. Qian, *Energy Storage Mater.*, 2020, **26**, 223–233.
25 S. Zhao, J. Zhang and L. Fu, *Adv. Mater.*, 2021, **33**, 2005544.
26 T. Imajo, T. Suemasu and K. Toko, *Sci. Rep.*, 2021, **11**, 8333.
27 S. Rezayati and A. Morsali, *Inorg. Chem.*, 2024, **63**, 6051–6066.
28 Y. Li, X. Bao, X. Wang, J. Zhao, P. Chen, H. Liu, H. Wang, L. Sun and W. Liu, *ACS Appl. Nano Mater.*, 2023, **6**, 18780–18789.
29 S. Samanta, S. Z. Rahaman, A. Roy, S. Jana, S. Chakrabarti, R. Panja, S. Roy, M. Dutta, S. Ginnaram, A. Prakash, S. Maikap, H.-M. Cheng, L.-N. Tsai, J.-T. Qiu and S. K. Ray, *Sci. Rep.*, 2017, **7**, 11240.
30 L. Sun, J. Xie, S. Huang, Y. Liu, L. Zhang, J. Wu and Z. Jin, *Sci. China Mater.*, 2022, **65**, 51–58.
31 S. Fang, L. Shen, G. Xu, P. Nie, J. Wang, H. Dou and X. Zhang, *ACS Appl. Mater. Interfaces*, 2014, **6**, 6497–6503.
32 H. Kim, Y. Son, C. Park, M.-J. Lee, M. Hong, J. Kim, M. Lee, J. Cho and H. C. Choi, *Nano Lett.*, 2015, **15**, 4135–4142.
33 F. Meng, F. Wang, H. Yu, Z. Zhao, Y. Lv, C. Ma, D. Zhang and X. Liu, *ACS Appl. Energy Mater.*, 2021, **4**, 14575–14581.
34 Y. Chen, P. Li, M. Huang, C. Wu, Q. Huang, T. Xie, X. Lin, A. Zeb, Y. Wu, Z. Xu and Y. Cai, *J. Energy Chem.*, 2024, **98**, 180–195.
35 Z. Zhao, J. Han, F. Chen, J. Xiao, Y. Zhao, Y. Zhang, D. Kong, Z. Weng, S. Wu and Q.-H. Yang, *Adv. Energy Mater.*, 2022, **12**, 2103565.
36 J. Sang, C. Sun, J. Pan, C. Gao, R. Zhang, F. Jia, F. Wang and Q. Wang, *ACS Appl. Mater. Interfaces*, 2024, **16**, 11389–11399.
37 M. Qorbani, A. Esfandiar, H. Mehdipour, M. Chaigneau, A. Irajizad and A. Z. Moshfegh, *ACS Appl. Energy Mater.*, 2019, **2**, 3665–3675.
38 R. Zhang, P. Yu, Z. Li, X. Shen, Y. Yu and J. Yu, *Small*, 2024, 2407276.
39 J. Y. Kim, S. Jung, S. H. Kang, J. Park, M. J. Lee, D. Jin, D. O. Shin, Y.-G. Lee and Y. M. Lee, *Adv. Energy Mater.*, 2022, **12**, 2103108.
40 J. Fu, D. Wang, Y. Li, X. Liu, R. Zhang, Z. Liu, P. Liu, L. Zhang, X. Li and G. Wen, *Nano Res.*, 2024, **17**, 2693–2703.

